ACS OMEGA

http://pubs.acs.org/journal/acsodf

Article

Boosted Mechanical Piezoelectric Energy Harvesting of Polyvinylidene Fluoride/Barium Titanate Composite Porous Foam Based on Three-Dimensional Printing and Foaming Technology

Cheng Yang, Fang Chen, Jingyao Sun, and Ning Chen*

Cite This: *ACS Omega* 2021, 6, 30769−30778

Read Online

ACCESS | Metrics & More | Article Recommendations | Supporting Information

ABSTRACT: The popularity of intelligent and green electronic devices means that the use of renewable mechanical energy has gradually become an inevitable choice for social development. However, it is difficult for the existing energy harvesters to meet the requirement for efficient collection of discrete mechanical energy due to the limitation of traditional two-dimensional (2D) film deformation. In this research, a green and convenient supercritical carbon dioxide foaming (Sc-CO_2)-assisted selective laser sintering method was developed, and piezoelectric energy harvesters with a 3D porous structure of polyvinylidene fluoride (PVDF)/barium titanate ($BaTiO_3$) were successfully constructed. The 3D structure combined with the porous structure made full use of the normal space, amplified the stress−strain effect, and improved the piezoelectric output capability. Under the synergistic effect of $BaTiO_3$, the foams exhibited high output with an output voltage of 20.9 V and a current density of 0.371 nA/mm^2, which exceeded most of the known PVDF/$BaTiO_3$ energy harvesters, and the prepared piezoelectric energy harvester could directly light up 11 green light-emitting diodes and charge a 1 μF commercial capacitor to 4.98 V within 180 s. This work emphasizes the key role of 3D printing and Sc-CO_2 foaming in fabricating 3D piezoelectric energy harvesters.

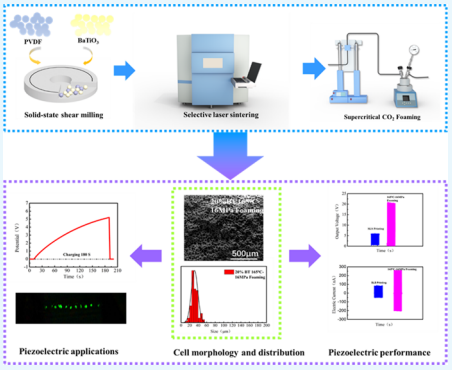

INTRODUCTION

In the 21st century, to meet the global demand for sustainable, low-carbon development, the application of safe and clean energies such as solar energy, wind energy, thermal energy, and mechanical energy becomes more and more indispensable.[1−3] A piezoelectric nanogenerator can convert a large amount of irregular mechanical energy into useful electrical energy in various ways, which is a new type of intelligent energy.[4−6] Nevertheless, traditional piezoelectric devices based on mechanical energy capture are mostly 2D thin structures,[7] which are of little help to the amplification of piezoelectric output,[8] because film products can only provide transverse and longitudinal strains while ignoring normal strains.[9,10]

In order to overcome the above drawback and take advantage of the normal space to generate greater piezoelectric strain, the construction of a 3D structure is imperative.[11,12] The current research methods widely used in fabricating 3D piezoelectric structures are mainly focused on the emerging 3D printing.[13,14] For instance, Liu et al.[15] successfully prepared 3D energy harvesters by fused deposition molding technology, and their piezoelectric output voltage was 4.7 times higher than that of planar energy harvesters. Wang et al.[16] showed a novel PA11/$BaTiO_3$/graphene ternary nanocomposite part with a discontinuous graphene network and micropores by selective laser sintering (SLS) technology, which obtained a d_{33} of 3.8 pC/N and a piezoelectric voltage of 16.2 V. Regrettably, although changes in the macrostructure can improve strain to a certain extent, there is still much room for improvement in piezoelectric output for components with a high modulus.[17] Fortunately, studies have shown that porous structure can improve the output sensitivity of piezoelectric materials because lowering the modulus of the material can increase the piezoelectric response.[18−21] For example, Mao et al.[21] designed a mesoporous piezoelectric PVDF film by the template method, and the piezoelectric output was twice of that of the ordinary piezoelectric film. Song et al.[22] used PVDF as a material to construct an interesting multilayer foam structure through immersion shear grinding and salt technology, and the highest piezoelectric output reached 11.8 V and 217.8 nA. However, how to combine the macrostructure design of 3D printing with the advantages of the low modulus of the porous structure to solve the low efficiency in collecting discrete mechanical energy is still a key issue.

At present, Sc-CO_2 foaming is a green and convenient emerging method for preparing porous foams, which is widely

Received: September 9, 2021
Accepted: October 26, 2021
Published: November 2, 2021

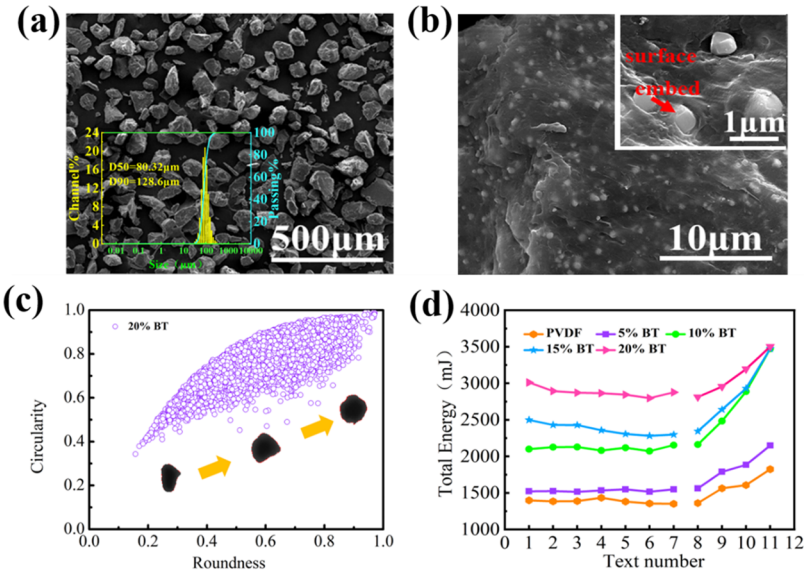

Figure 1. (a,b) SEM images of 20% BT powders under different magnifications (the inset shows the size distribution), (c) corresponding circularity−roundness relationship of 20% BT powders, and (d) test curves of stability and sensitivity to flow rates.

used in electromagnetic shielding, oil−water separation, and so on.[23,24] However, the application of supercritical foaming technology in the piezoelectric field is still very few. This may be due to the long adsorption time of CO_2 by piezoelectric polymers such as PA11 and PVDF. Comfortingly, the special structure formed by 3D printing can perfectly solve this problem.[25] Thus, a foam with different pore distributions can be controlled and the microstructure is optimized by Sc-CO_2 foaming, on the basis of applying 3D printing to build a macrostructure,[26] which provides a new strategy for constructing microporous piezoelectric foams.

PVDF is a widely used piezoelectric polymer material with suitable mechanical and piezoelectric properties.[27] However, the piezoelectric properties of PVDF still have a certain gap compared with piezoelectric ceramics in practical applications.[28,29] Fortunately, the introduction of lead-free $BaTiO_3$ in an appropriate amount can effectively solve this problem. In this study, a novel method for preparing piezoelectric energy harvesters with a 3D porous structure with solid-state shear milling (S^3M), SLS, and Sc-CO_2 foaming was proposed. First, different contents of the PVDF/$BaTiO_3$ composite material were prepared by S^3M technology, and the $BaTiO_3$ nanoparticles were uniformly dispersed in a PVDF matrix. Second, the complete external 3D structure was successfully constructed by SLS, and the internal porous structure provided a prerequisite for subsequent processing. Finally, the internal regular pore structure was perfectly fabricated through Sc-CO_2 foaming, which amplified the piezoelectric output effectively. This research not only improves the application of PVDF/$BaTiO_3$ in the piezoelectric direction but also broadens the way for the construction of 3D foams.

RESULTS AND DISCUSSION

Characterization of PVDF/$BaTiO_3$ Powders. The SEM micrographs of Figure 1a and Figure S1 fully reflected the irregular but nearly spherical shape of the four composite powders used for sintering. It could be seen from the high-magnification SEM image (Figure 1b) that the powders showed a certain degree of roughness, and the $BaTiO_3$ nanoparticles were attached to the surface or embedded in the PVDF matrix under the strong 3D shear force field of the disc mill[30] without obvious agglomeration. Experiments had proven that S^3M technology could provide uniform dispersion and enhance the PVDF/$BaTiO_3$ interface interaction, which is the basic condition for obtaining high-voltage electrical properties.[31] The particle size is another key factor affecting the sintering stability of SLS. Powders with a too small particle size are difficult to spread, while powders with a too large particle size are difficult to be sintered, so the optimal sintering particle size range is 10−150 μm.[32] The particle size and distribution of PVDF/$BaTiO_3$ powders prepared in this paper are shown in the inset of Figure 1a and Figure S1. Their D_{90} were 101.4, 82.52, 100.9, and 128.6 μm, which met the optimal particle size range required by SLS.

Spherical powders have the characteristics of low surface energy and a small contact area, which not only can effectively avoid agglomeration and electrostatic adsorption but also ensure excellent fluidity and high bulk density.[33,34] Therefore, it is necessary to build spherical or nearly spherical powders to meet the requirements of SLS processing to reduce the structural defects of the workpiece and increase the material utilization rate. Based on the qualitative observation of the powder morphology with SEM, a dynamic particle image measuring device was further used to quantitatively describe the geometric parameters of the powders and analyze the geometric characteristics of the powders, which can provide various characteristic parameters such as roundness, circularity, etc. The circularity of the 20% BT powder particles had a certain corresponding relationship with the roundness, as shown in Figure 1c. The results showed that the powders had high circularity and roundness, indicating that the outline of the powders was round and the shape was close to spherical, which is consistent with the SEM image. Figure 1d compared the stability and sensitivity of different powders to flow rates. According to the test curve, it could be seen that the flow energy of the $BaTiO_3$-added powders had increased. This may be due to the introduction of $BaTiO_3$, which improved the compactness of the powders, increased the bulk density, and reduced the porosity. Therefore, the resistance to exercise was greater, and the energy required increased accordingly. By the

https://doi.org/10.1021/acsomega.1c04998
ACS Omega 2021, 6, 30769−30778

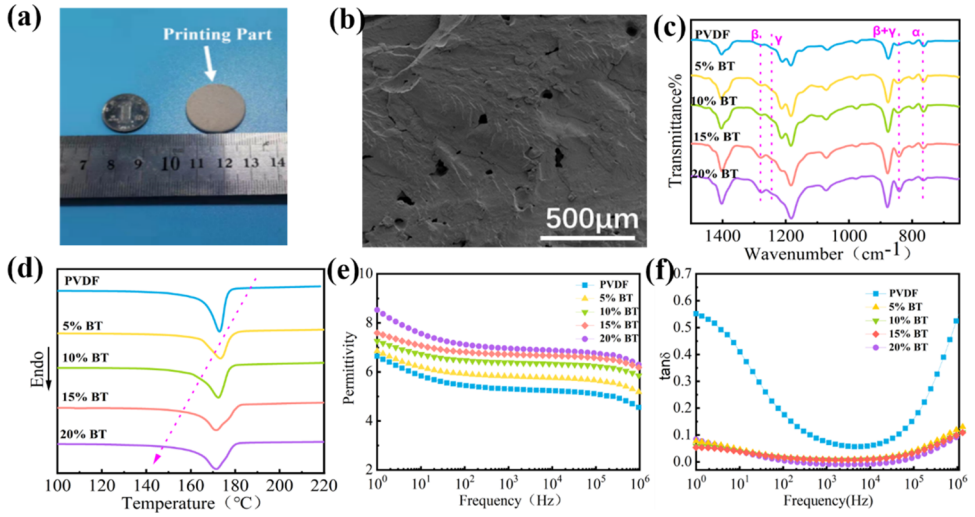

Figure 2. (a) Digital photo and (b) SEM image of the 20% BT SLS part, (c) FT-IR spectra and (d) DSC curves of SLS parts, and (e,f) frequency-dependent dielectric responses.

way, the crystal form of the composite material has also been analyzed, and the results show that there is almost no difference from pure PVDF (Figure S2).

Performance Characterization of PVDF/$BaTiO_3$ Sintered Parts. The physical photo of the sintered part in Figure 2a presented that the printed part had a clear outline and high dimensional accuracy. Meanwhile, the part did not show any warpage and sintering allowance, which indicated that the powder's particle size, printing temperature, sintering power, and other parameters were all within the optimal value range. Moreover, the micropores were created inside the parts due to sintering of the composite particles (Figure 2b), which could enhance the pressure sensitivity and flexibility of the piezoelectric materials. In this study, these micropores were also conducive to the entry of Sc-CO_2 in the later stage to help for the postfoaming process.[25]

FT-IR could be used to characterize the crystal phases in the parts, and the curves are shown in Figure 2c. The vibrational peaks at 840 and 1279 cm^{-1} correspond to the β phase, while the peaks at 766 cm^{-1} belong to the α phases.[35] It is confirmed from the FT-IR spectrum that the peak intensities of the composite materials at 840 and 1279 cm^{-1} were correspondingly stronger than those of pure PVDF, which proved that the content of the β crystal phase in the powders with $BaTiO_3$ was relatively higher. Here, it is worth noting that the 1234 cm^{-1} vibration peak belonging to the γ phase[36] is not shown in Figure 2c, indicating that the piezoelectric crystal phase of the composite powders was all β phases. The above results preliminarily explained that introducing $BaTiO_3$ was conducive to improving the β phase of PVDF, and the reason for this phenomenon could be explained by the heterogeneous nucleation of $BaTiO_3$. Melting curves (Figure 2d) revealed that all the samples only presented one single peak with the melting point ranging from 170 to 172 °C, confirming the predominant role of the β phase once more.[37] The dielectric properties of the composites are presented in Figure 2e,f. $BaTiO_3$ with a high dielectric constant caused charge accumulation under the action of an electric field, thus strengthening the interface polarization effect. The increase in the dielectric constant and the decrease in the dielectric loss indicated that composite materials had an enhanced charge-binding ability, which is crucial for improving piezoelectric properties and power−electricity conversion efficiency.[38]

Foaming Behaviors of PVDF/$BaTiO_3$ Printed Parts. Figures S3 and S4 show the pore morphology and piezoelectric output under different foaming parameters, respectively. It can be seen that the increase in temperature made the pore size expand, but the pore would collapse when the temperature was too high; meanwhile, the enhancement in foaming pressure significantly affected the pore density.[39] After a series of experiments, we determined that the optimal foaming parameters of all printed parts were 165 °C and 16 MPa. Figure 3a−e shows the SEM images of the 3D porous structure

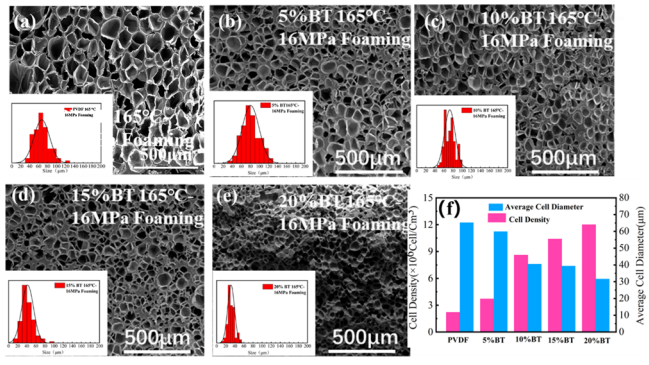

Figure 3. Cross-sectional SEM pictures of foamed parts. (a) PVDF, (b) 5% BT, (c) 10% BT, (d) 15% BT, and (e) 20% BT; the insets show the corresponding pore diameter distribution. (f) Average pore diameter and pore density of PVDF and PVDF/$BaTiO_3$ parts.

and the density statistics of the foams under the optimal foaming parameters. At the same foaming temperature and pressure, increasing the content of inorganic fillers had a great influence on the foaming process. First of all, the well-dispersed $BaTiO_3$ particles underwent heterogeneous nucleation in the PVDF matrix, thereby effectively reducing the critical free energy barrier during foaming and increasing the pore density. Second, the introduction of $BaTiO_3$ effectively enhanced the strength of the porous wall, stabilized the pore structure, and prevented pore deterioration under the action of the tensile force generated during pore growth. The pore

https://doi.org/10.1021/acsomega.1c04998
ACS Omega 2021, 6, 30769−30778

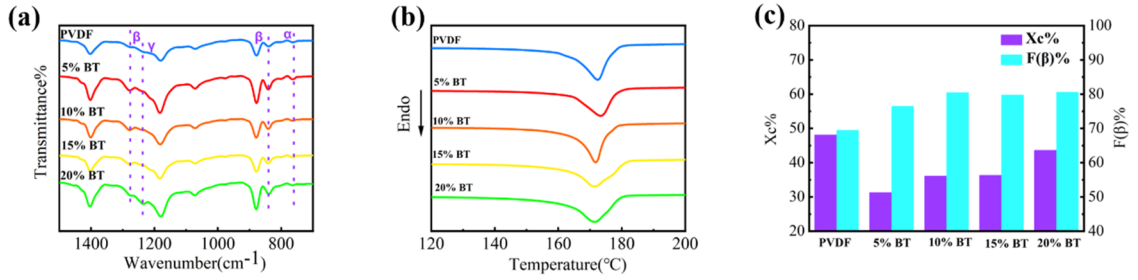

Figure 4. Crystal analysis of parts. (a) FT-IR and (b) DSC curves of the foams at different contents of $BaTiO_3$ and (c) crystallinity and β crystal content of foams.

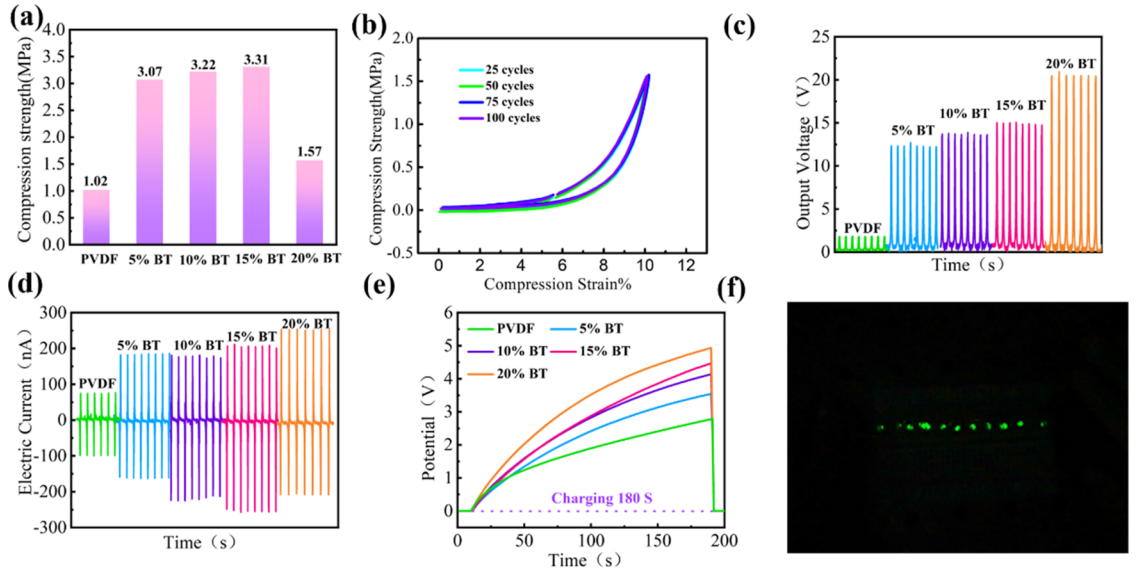

Figure 5. (a) Compressive properties of foam parts under 10% deformation (50 cycles) and (b) compressive strength diagram of the 20% BT foam sample under different cycles. Open-circuit voltage (c) and short-circuit current (d) diagram of foam at different contents of $BaTiO_3$, (e) comparison of energy storage properties of samples, and (f) physical photo of driving 11 LED bulbs with the 20% BT foam.

distribution shown in Figure 3f further proved the above conclusions. Under definite conditions, the 5−20% $BaTiO_3$ foamed parts have average pore diameters of 59.9, 50.5, 39.3, and 31.6 μm and pore densities of 3.7×10^6, 8.6×10^6, 10×10^6, and 12×10^6 cells/cm^3, respectively. Meanwhile, the average pore diameter of pure PVDF foam was only 65.2 μm, and the cell density was 1.7×10^6 cells/cm^3. However, excessive ceramics would prevent the formation and growth of pores, resulting in the incomplete appearance of foamed parts (as shown in Figure S5).

The crystal phases in the 3D porous structure foams were evaluated by combining FT-IR and DSC characteristics (revealed in Figure 4). As expected, the FT-IR spectra proved the dominant role of the piezoelectric phase in all the investigated samples shown in Figure 4a. For instance, in FT-IR patterns, intensity peaks related to the β or γ phase (840 cm^{-1}) could be detected in all foams, which could be explained as that the pore growth and expansion process was similar to stretching, making the PVDF molecular chain change from a stable TGTG′ (α phase) to TTTT (β phase) or TGTG (γ phase) conformation.[37] Interestingly, the characteristic absorption peak of the γ phase at 1234 cm^{-1} was also shown in the 20% BT foam curve, which was different from the other curves. The appearance of this phenomenon was related to the movement of the PVDF molecular chain. During the foaming process, the nondirectional interaction between ceramic particles and the polymer hindered the formation of the long-trans TTTT conformation, and the PVDF crystal underwent a small degree of the $\alpha \rightarrow \gamma$ transition. Fortunately, the only melting peak below 175 °C appeared in the DSC curve (Figure 4b), indicating that under the optimal foaming parameters, the β crystal phase occupied a dominant position. As shown in Figure 4c, the β phase content of pure PVDF foam was 69.5%, but when the mass fraction of $BaTiO_3$ reached 20 wt %, the β phase content increased to 80.6%, which was due to polarized $BaTiO_3$ inducing the self-polarization of the PVDF matrix, leading to the nucleation of the electroactive β phase in the foam during the polarization process.[40] Apart from the piezoelectric crystal content, crystallinity (X_c) was another essential factor determining the piezoelectricity of PVDF. Generally, the crystallization was divided into two processes: nucleus formation and grain growth, and the final crystallinity of composites was determined by the competition of the two effects.[41] Compared with pure PVDF foamed parts, the crystallinity of the composite foam has been significantly reduced. For example, the crystallinity of the former was 48.1%, and the crystallinity of the latter was only 30−45%. This is probably because the blocking effect played an outstanding role when the filler was added. However, only comparing the crystallinity of foams with different $BaTiO_3$ contents, the crystallinity increased steadily as the filler content increased. From a certain

https://doi.org/10.1021/acsomega.1c04998
ACS Omega 2021, 6, 30769−30778

perspective, the denser pore structure had a more obvious effect on the stretching orientation of molecular chains during the formation process, which would promote the increase in crystallinity.[53] For instance, the maximum crystallinity of the 5% BT foaming part was around 30 wt %, while that of the composite foam containing 20 wt % was around 44 wt %.

Piezoelectricity of PVDF/$BaTiO_3$ Foamed Parts. The compression performance of the 3D porous piezoelectric parts was fully expressed in Figure 5a,b. Compared with pure PVDF foam, the compressive strength of PVDF/$BaTiO_3$ composite foam had been significantly improved, attributed to the higher pore density. When the $BaTiO_3$ content was enhanced to 15%, the compressive strength of the composite foamed part increased to 3.31 MPa, which was 2.29 MPa higher than that of the pure foamed part. However, the 20% BT porous parts illustrated a lower compression modulus with the same 10% compression, which was directly related to its pore morphology. The result showed that the enhancement in pore density would cause the compression strength to decrease. As a proof of concept, we could also explain it as follows: when the pore size was small, the compaction distance was shorter and the stress transfer was accelerated, while the larger pore diameter extended the compaction distance, which unexpectedly showed a greater compressive strength. The cyclically compressed image of the 20% BT foam at the foaming parameters of 165 °C and 16 MPa is shown in Figure 5b. Obviously, the foaming parts showed good reversibility, outstanding compressibility, and remarkable stability during compression processes.

The open-circuit voltage and short-circuit current are two important indicators to measure the power-to-electricity conversion capability of piezoelectric components. In order to explore the piezoelectric properties of different PVDF/$BaTiO_3$ foams, the open-circuit voltage and short-circuit current of each foamed part were tested with a linear motor under the condition of 5 m/s^2, as shown in Figure S6. It could be seen intuitively from Figure 5c,d that the open-circuit voltage and short-circuit current of the 3D porous structure showed a continuous increasing trend, and the reason can be stated as follows: (1) Obviously, the 20% BT foam had more ceramics, which significantly helped the increase in piezoelectric output.[42] (2) The 20% BT foam with high pore density and a low compressive modulus could generate a greater strain in the normal space, thereby improving the piezoelectric conversion efficiency.[43] (3) The 20% BT foam with a denser pore structure naturally formed more electrets under the polarization condition of 8 kV, which was of great benefit to the stored charge.[44] (4) During the foaming process, the 20% BT foam formed more piezoelectric crystal phases, which was beneficial to improving the mechanical and electrical coupling capabilities of the parts, even if the effect of this point was significantly smaller than the above three. Comfortingly, our work not only revealed the promising future in the electronic applications of PVDF/$BaTiO_3$ nanocomposite foams but also provided a new direction for the research in the field of piezoelectrics for 3D porous structures. Furthermore, the practical applications of the energy harvesters with a 3D porous structure in the energy harvesting and charging capabilities were tested by this article. The output voltage of the 20% BT foam reached 20.9 V at an acceleration rate of 5 m/s^2, which could light up 11 LEDs easily, as shown in Figure 5f. Not only that, a 1 μF capacitor could be successfully charged to a maximum of 4.98 V in 180 s by designing a bridge rectifier to convert alternating current to direct current (Figure 5e).

As an energy harvester with excellent capture performance, discrete mechanical energy generated by the irregular movement of the human body in daily life can also be widely collected, in addition to the continuous impact of linear motors. Here, we chose the 20% BT foam samples for piezoelectric application testing in human motion mode, including finger pressing, fist hitting, and pedaling, etc. Figure 6a–d shows that the composite foam had high sensitivity and a strong collection ability and could adapt to human movements of different frequencies and amplitudes. For example, when the finger pressed lightly, the maximum output voltage could reach ~7 V, while under jumping conditions, the output voltage was close to 25 V, which proves the powerful application prospect of piezoelectric foam in the collection of discrete mechanical energy. Impressively, the response time and sensitivity of the final foam part are also evaluated, that is, 70 ms and 0.0331 V/N (Figures S7 and S8), respectively, which proved that there is a promising application prospect in the field of sensing.

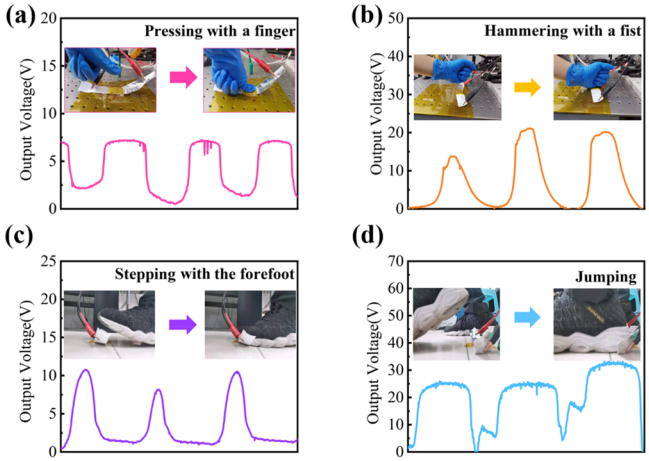

Figure 6. Ability to convert human motions into piezoelectric output: (a) pressing with a finger, (b) fist hammering, (c) stepping with the forefoot, and (d) jumping.

Figure 7a,b compares the open-circuit voltage and short-circuit current of the three processing methods of molding, SLS, and foaming, respectively. The open-circuit voltage obtained through SLS was increased by 2 times, and the short-circuit current was increased by 2.7 times compared with the molding method. The main reason could be attributed to the special pore structure formed during the SLS sintering process as mentioned earlier, which helped to expand the piezoelectric output. More surprisingly, it could be seen that the voltage and current outputs of the parts with the 3D porous structure studied in this paper were 8.1 and 8.7 times that of the molded one, respectively. This showed that the uniform pore structure can effectively use the normal space and improve the power-to-electricity conversion capacity of the parts.

The foam compression schematic (Figure 7c) further proved that the pore structure contributes to the improvement of compression deformation, which was very beneficial to the increase in piezoelectric output, attributed to the porous 3D structure. The 3D foam model could make the compressive stress uniformly distributed in the vertical direction, which significantly reduces the clamping effect.[45] As a proof of

https://doi.org/10.1021/acsomega.1c04998
ACS Omega 2021, 6, 30769−30778

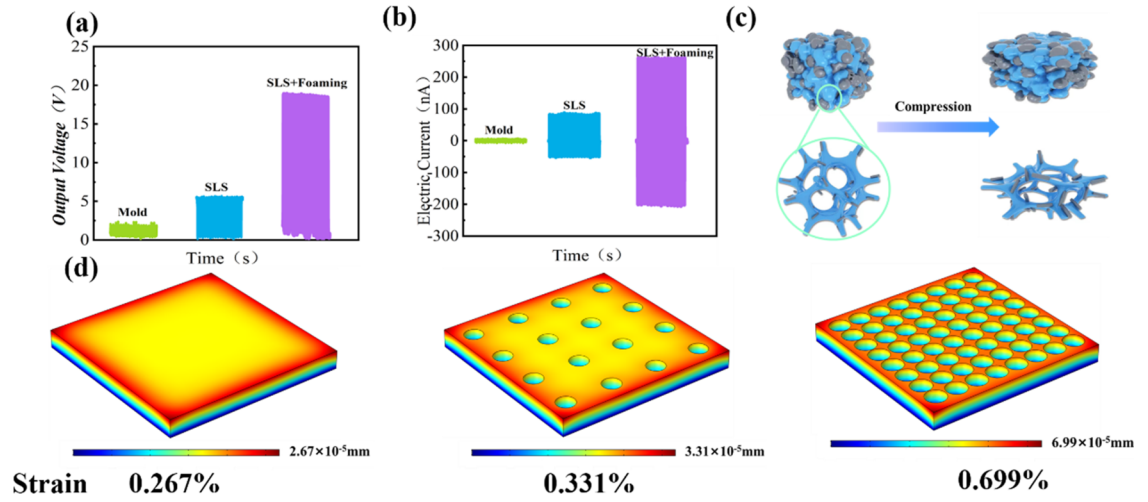

Figure 7. Open-circuit voltage (a) and short-circuit current (b) diagrams of the mold part, SLS parts, and foam; (c) schematic of the structural change in the foaming part during compression; (d) simulation results of foams with different porosities.

concept, the COMSOL simulation system was used to compare the compressive strains of flat, low-porosity, and high-porosity parts, which were 0.267, 0.331, and 0.699%, respectively (the simulated parts had the same pore size, and the applied pressure was 2 N). The results show that the increase in porosity will lead to strain accumulation, which has great potential in the field of piezoelectric output (Figure 7d).

It is worth noting that this article selected the PVDF/$BaTiO_3$ composite piezoelectric parts reported in recent years for comparison. In general, the 3D energy harvester with a porous structure has high piezoelectric output performance, which is better than the PVDF/$BaTiO_3$ piezoelectric composite devices formed by most of the processing techniques (blue area in Figure 8),[46−52] such as spin-coating.

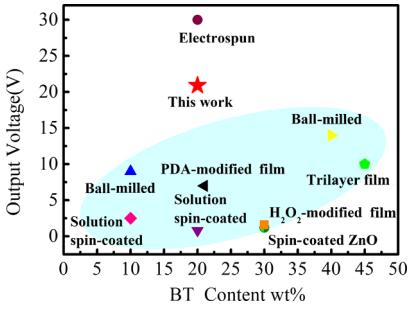

Figure 8. Comparison of output capacities between this work and others.

Notably, our work achieved a larger piezoelectric output with a relatively low filler addition, which opens a new door for the construction of piezoelectric energy equipment.

CONCLUSIONS

All in all, the 3D, flexible, and high-performance piezoelectric foams were successfully fabricated by integrating S^3M, SLS printing, and Sc-CO_2 foaming. Based on the strong shearing function of S^3M equipment, PVDF/$BaTiO_3$ composite powders with uniform dispersion were obtained and met the requirements for SLS printing. PVDF/$BaTiO_3$ piezoelectric foams were successfully achieved through SLS and Sc-CO_2. The 3D porous structure with surface integrity and dense porosity is an ideal model to improve piezoelectric performance, which could amplify the stress and strain response while making full use of the normal space. In addition, the coupling effect of piezoelectric ceramics and porous electrets had an indispensable benefit for improving the piezoelectric output capability, which displays an output voltage of 20.9 V and a current density of 0.371 nA/mm^2. Impressively, a PVDF-based piezoelectric energy harvester can directly light up 11 green LEDs and charge a capacitor to 4.98 V within 180 s. This green and convenient method of manufacturing piezoelectric foams opens a new door to enrich the theory and application of 3D piezoelectric research.

EXPERIMENTS AND CHARACTERIZATION

Materials. PVDF particles (FR906) with a melting point of 172 °C were purchased from the Shanghai Sanaifu New Material Technology Co., Ltd., China.

$BaTiO_3$ (average particle size of 500 nm, tetragonal crystal phase) was supplied by the Shandong Sinocera Functional Material Co., Ltd., China.

Carbon dioxide (99.5%) was supplied by the China Chengdu Taiyu Natural Gas Company.

Preparation of PVDF/$BaTiO_3$ Composite Powders. PVDF with different contents of $BaTiO_3$ (the mass fractions of $BaTiO_3$ were 5, 10, 15, and 20%, respectively) was preliminarily mixed, and then, the mixture was added to S^3M equipment (MF-400 frequency conversion type, Chengdu Pumeiyi Technology Co., Ltd., China) and milled 10 times, with the speed of the grinding disc controlled to be 30−40 rpm. Second, the as-prepared PVDF/$BaTiO_3$ compounded powders were extruded at 190−210 °C through a corotating twin-screw extruder (RM-200C, Harbin HAPRO Electric Technology Co., Ltd., China). Then, the pellets were crushed in liquid nitrogen and dried in a vacuum oven at 80 °C for 8 h. In order to remove the coarser and smaller powder particles, the powders were sieved with 150 and 300 mesh sieves to obtain those with a certain particle size for SLS and then designated them as 5, 10, 15, and 20% BT.

Sintering of PVDF/$BaTiO_3$ Powders. PVDF/$BaTiO_3$ composite powders were sintered through SLS equipment (HT 251P, the Hunan Farsoon High-Tech Co., Ltd., China), with a preheating powder bed at 155 °C, a laser power of 40

https://doi.org/10.1021/acsomega.1c04998
ACS Omega 2021, 6, 30769−30778

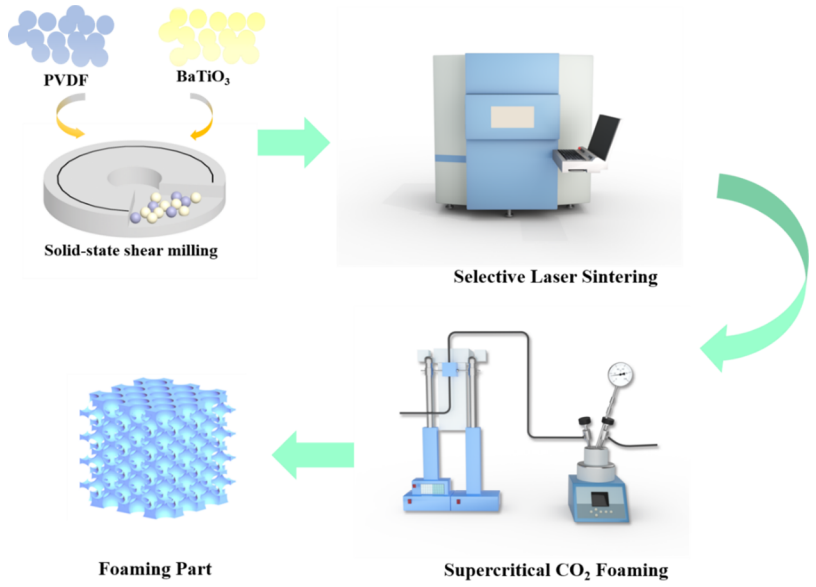

Figure 9. Schematic diagram of the preparation of PVDF/$BaTiO_3$ foamed parts.

W, a scanning distance of 0.1 mm, a scanning speed at 9600 mm/s, and a powder layer of 0.1 mm. After sintering, the powders were cooled to room temperature, and the parts were taken out, which were still called the above names (5, 10, 15, and 20% BT).

Sc-CO_2 Foaming of PVDF/$BaTiO_3$ Sintered Parts. The PVDF/$BaTiO_3$ sintered parts were placed into a mold and saturated with Sc-CO_2 at 50 °C and 7 MPa for 2.5 h, which was rapidly heated to 165 °C and 16 MPa within 30 min and then quickly depressurized to obtain foams. The foamed parts were also called 5, 10, 15, and 20% BT. The processing of the foamed parts is shown in Figure 9.

Characterization. The particle size and particle size distribution of PVDF/$BaTiO_3$ particles were determined by a size measuring device (S3500, Microtrac, USA). The PVDF/$BaTiO_3$ particles should be uniformly dispersed in an ethanol solvent and ultrasonicated for about 5 min to obtain a uniformly dispersed suspension. The flow stability of the composite powders was analyzed by an FT4 powder rheometer (Freeman Technology Co., Ltd., UK).

An SEM (INSPECT F, FEI, Japan) was used to analyze the morphology of the PVDF/$BaTiO_3$ foam samples. After the samples were soaked for 10 min and quenched, the quenched section was vacuum sprayed with gold. The powder morphology, cross-sectional morphology after SLS sintering, cross-sectional pore morphology, pore density, etc. could be observed. The formula for calculating pore density was as follows[55]

$$N = \left(\frac{nM^2}{A}\right)^{3/2} \tag{1}$$

n represents the number of pores in the SEM micrograph, A represents the area of the micrograph, and M represents the magnification factor.

An FT-IR (Nicolet 6700 Fourier transform infrared spectrometer from Thermo Scientific, USA) could identify different crystal forms and the content of each crystal form in PVDF/$BaTiO_3$ powders and parts. In addition, the FT-IR could also be used to determine the crystal form conversion during the SLS and Sc-CO_2 foaming processes. The specific method was to test the samples under 2 mm in the ATR mode. According to the Lambert−Beer law to estimate the relative β phase fraction ($F(\beta)$), it could be expressed by[54]

$$F(\beta) = \frac{X_\beta}{X_\beta + X_\alpha} = \frac{A_\beta}{(K_\beta/K_\alpha)A_\alpha + A_\beta} \tag{2}$$

A_α and A_β indicate the absorption peaks at 766 and 840 cm^{-1}, respectively, and K_α and K_β indicate the absorption coefficients of the sample, that is, $K_\alpha = 6.1 \times 10^4$ cm^2 mol^{-1} and $K_\beta = 7.7 \times 10^4$ cm^2 mol^{-1}.

The crystallinity and melting point of the composite powders during the SLS and Sc-CO_2 foaming processes could be measured by DSC (Q20 from TA Company, USA). This process was mainly to load approximately 7 mg of the sample into a crucible, increase the temperature from 40 to 230 °C at a rate of 10 °C/min, and then decrease the temperature to 40 °C. The crystallinity X_c could be calculated by the following formula[55]

$$X_c = \frac{\Delta H_m}{\Delta H_{100\%}} \times 100\% \tag{3}$$

$\Delta H_{100\%}$ represents the melting enthalpy of complete crystallization of the polymer, and ΔH_m represents the melting enthalpy measured by DSC. Here, $\Delta H_{100\%} = 105$ J/g.

The crystal shape of the milled powders was determined by X-ray diffraction (XRD) (Ultima IV, RIGAKU, Japan) at a scanning speed of 10°/min and a scanning step of 0.01° at 5−80°.

A broadband dielectric impedance relaxation spectrometer (Concept50, Novocontrol GmbH, Germany) was used to test the dielectric constant and dielectric loss of the sample. It was used to indicate the relationship between the dielectric properties of the powders and the change in the $BaTiO_3$ content. The test frequency was 10^0−10^6 Hz.

An Electro Force 3220 (Bose Company, USA) was used to test the cyclic compression performance of the parts. The cycle period and the compression deformation were 100 cycles and 10%, respectively.

https://doi.org/10.1021/acsomega.1c04998
ACS Omega 2021, 6, 30769−30778

The specific test procedures for piezoelectric properties (NTI AG HS0137×166, China) were as follows: we coated both sides of the wafer uniformly with conductive silver glue, dried them, and used a polarization instrument to load a high-voltage 8 kV/mm polarization in an 80 °C silicone oil bath for 30 min. After polarization, the piezoelectric output capability test was performed. It should be noted that its position needs to face the impact head. The linear motor hit, the sheet at 5 m/s^2, and the open-circuit voltage as well as the short-circuit current of the foamed part were amplified and outputted to the computer.

■ ASSOCIATED CONTENT

Supporting Information

The Supporting Information is available free of charge at https://pubs.acs.org/doi/10.1021/acsomega.1c04998.

SEM and particle size distribution of the composite powders; characterization of the crystal form of the composite powders; cell morphology and piezoelectric output with different foaming parameters; digital photo of the PVDF/30% $BaTiO_3$ foaming part and piezoelectric test equipment; foam response time and sensitivity test (PDF)

■ AUTHOR INFORMATION

Corresponding Author

Ning Chen − *State Key Laboratory of Polymer Materials Engineering (Sichuan University), Polymer Research Institute, Sichuan University, Chengdu 610065, China*; Email: ningchen@scu.edu.cn

Authors

Cheng Yang − *State Key Laboratory of Polymer Materials Engineering (Sichuan University), Polymer Research Institute, Sichuan University, Chengdu 610065, China*; orcid.org/0000-0002-3748-9765

Fang Chen − *State Key Laboratory of Polymer Materials Engineering (Sichuan University), Polymer Research Institute, Sichuan University, Chengdu 610065, China*

Jingyao Sun − *State Key Laboratory of Polymer Materials Engineering (Sichuan University), Polymer Research Institute, Sichuan University, Chengdu 610065, China; State Key Laboratory of Organic-Inorganic Composites and College of Mechanical and Electrical Engineering, Beijing University of Chemical Technology, Beijing 100029, China*; orcid.org/0000-0002-0140-0212

Complete contact information is available at: https://pubs.acs.org/10.1021/acsomega.1c04998

Notes

The authors declare no competing financial interest.

■ ACKNOWLEDGMENTS

This work is supported by the National Natural Science Foundation of China (51933007 and 51720105012), the National Key R&D Program of China (2017YFE0111500), the Program for Featured Directions of Engineering Multi-disciplines of the Sichuan University (no. 2020SCUNG203), and the Opening Project of the State Key Laboratory of Polymer Materials Engineering (Sichuan University) (no. sklpme 2020-4-09).

■ REFERENCES

(1) Wang, J.; Jiang, J.; Zhang, C.; Sun, M.; Han, S.; Zhang, R.; Liang, N.; Sun, D.; Liu, H. Energy-efficient, fully flexible, high-performance tactile sensor based on piezotronic effect: Piezoelectric sigal amplified with organic field-effect transistors. *Nano Energy* **2020**, *76*, 105050.

(2) Peng, Z.; Chen, J.; Wang, C.; Li, W.; Zhang, B.; Cao, J.; Lu, J.; Wu, J.; Yang, W. Energy scavenging luminescent piezo-fabrics: small silicon dots enable big electrical outputs. *J. Mater. Chem. A* **2021**, *9*, 13231−13241.

(3) Zhang, D.; Fan, B.; Ying, L.; Li, N.; Brabec, C. J.; Huang, F.; Cao, Y. Recent progress in thick-film organic photovoltaic devices: Materials, devices, and processing. *SusMat.* **2021**, *1*, 4−23.

(4) Zhao, Q.; Yang, L.; Chen, K.; Ma, Y.; Peng, Q.; Ji, H.; Qiu, J. Flexible textured MnO_2 nanorods/PVDF hybrid films with superior piezoelectric performance for energy harvesting application. *Compos. Sci. Technol.* **2020**, *199*, 108330.

(5) Li, Y.; Xu, M.-h.; Xia, Y.-s.; Wu, J.-m.; Sun, X.-k.; Wang, S.; Hu, G.-h.; Xiong, C.-x. Multilayer assembly of electrospun/electrosprayed PVDF-based nanofibers and beads with enhanced piezoelectricity and high sensitivity. *Chem. Eng. J.* **2020**, *388*, 124205.

(6) Lv, J.; Chen, J.; Lee, P. S. Sustainable wearable energy storage devices self-charged by human-body bioenergy. *SusMat* **2021**, *1*, 285−302.

(7) Alluri, N. R.; Chandrasekhar, A.; Vivekananthan, V.; Purusothaman, Y.; Selvarajan, S.; Jeong, J. H.; Kim, S. J. Scavenging Biomechanical Energy Using High-Performance, Flexible $BaTiO_3$ Nanocube/PDMS Composite Films. *ACS Sustainable Chem. Eng.* **2017**, *5*, 4730−4738.

(8) Bhavanasi, V.; Kumar, V.; Parida, K.; Wang, J.; Lee, P. S. Enhanced Piezoelectric Energy Harvesting Performance of Flexible PVDF-TrFE Bilayer Films with Graphene Oxide. *ACS Appl. Mater.* **2016**, *8*, 521−529.

(9) Zhang, W.; Feng, Q.; Hosono, E.; Asakura, D.; Miyawaki, J.; Harada, Y. Tetragonal Distortion of a $BaTiO_3/Bi_{0.5}Na_{0.5}TiO_3$ Nanocomposite Responsible for Anomalous Piezoelectric and Ferroelectric Behaviors. *ACS Omega* **2020**, *5*, 22800−22807.

(10) Pan, C. T.; Wang, S. Y.; Yen, C. K.; Kumar, A.; Kuo, S. W.; Zheng, J. L.; Wen, Z. H.; Singh, R.; Singh, S. P.; Khan, M. T.; Chaudhary, R. K.; Dai, X. F.; Kaushik, A. C.; Wei, D. Q.; Shiue, Y. L.; Chang, W. H. Polyvinylidene Fluoride-Added Ceramic Powder Composite Near-Field Electrospinned Piezoelectric Fiber-Based Low-Frequency Dynamic Sensors. *ACS Omega* **2020**, *5*, 17090−17101.

(11) Ryu, J.; Kim, J.; Oh, J.; Lim, S.; Sim, J. Y.; Jeon, J. S.; No, K.; Park, S.; Hong, S. Intrinsically stretchable multi-functional fiber with energy harvesting and strain sensing capability. *Nano Energy* **2019**, *55*, 348−353.

(12) Song, S.; Li, Y.; Wang, Q.; Zhang, C. Boosting piezoelectric performance with a new selective laser sintering 3D printable PVDF/graphene nanocomposite. *Compos. Part A Appl. Sci. Manuf.* **2021**, *147*, 106452.

(13) Zhang, C.; Li, Y.; Kang, W.; Liu, X.; Wang, Q. Current advances and future perspectives of additive manufacturing for functional polymeric materials and devices. *SusMat* **2021**, *1*, 127−147.

(14) Tian, M.; Zhang, D.; Wang, M.; Zhu, Y.; Chen, C.; Chen, Y.; Jiang, T.; Gao, S. Engineering flexible 3D printed triboelectric nanogenerator to self-power electro-Fenton degradation of pollutants. *Nano Energy* **2020**, *74*, 104908.

(15) Liu, X.; Shang, Y.; Zhang, J.; Zhang, C. Ionic Liquid-Assisted 3D Printing of Self-Polarized β-PVDF for Flexible Piezoelectric Energy Harvesting. *ACS Appl. Mater.* **2021**, *13*, 14334−14341.

(16) Jin, Y.; Chen, N.; Li, Y.; Wang, Q. The selective laser sintering of a polyamide 11/$BaTiO_3$/graphene ternary piezoelectric nanocomposite. *RSC Adv.* **2020**, *10*, 20405−20413.

(17) Song, L.; Dai, R.; Li, Y.; Wang, Q.; Zhang, C. Polyvinylidene Fluoride Energy Harvester with Boosting Piezoelectric Performance through 3D Printed Biomimetic Bone Structures. *ACS Sustainable Chem. Eng.* **2021**, *9*, 7561−7568.

(18) Mahanty, B.; Ghosh, S. K.; Garain, S.; Mandal, D. An effective flexible wireless energy harvester/sensor based on porous electret piezoelectric polymer. *Mater. Chem. Phys.* **2017**, *186*, 327−332.
(19) Xu, Y.; Jin, L.; He, X.; Huang, X.; Xie, M.; Wang, C.; Zhang, C.; Yang, W.; Meng, F.; Lu, J. Glowing stereocomplex biopolymers are generating power: polylactide/carbon quantum dot hybrid nanofibers with high piezoresponse and multicolor luminescence. *J. Mater. Chem. A* **2019**, *7*, 1810−1823.
(20) Zhang, Y.; Bowen, C. R.; Deville, S. Ice-templated poly-(vinylidene fluoride) ferroelectrets. *Soft Matter* **2019**, *15*, 825−832.
(21) Mao, Y.; Zhao, P.; McConohy, G.; Yang, H.; Tong, Y.; Wang, X. Sponge-Like Piezoelectric Polymer Films for Scalable and Integratable Nanogenerators and Self-Powered Electronic Systems. *Adv. Energy Mater.* **2014**, *4*, 41301624.
(22) Song, L.; Huang, Z.; Guo, S.; Li, Y.; Wang, Q. Hierarchically Architected Polyvinylidene Fluoride Piezoelectric Foam for Boosted Mechanical Energy Harvesting and Self-Powered Sensor. *ACS Appl. Mater.* **2021**, *13*, 37252−37261.
(23) Feng, D.; Liu, P.; Wang, Q. Exploiting the piezoresistivity and EMI shielding of polyetherimide/carbon nanotube foams by tailoring their porous morphology and segregated CNT networks. *Compos. Part A Appl. Sci. Manuf.* **2019**, *124*, 105463.
(24) Li, J.; Zhang, G.; Fan, X.; Gao, Q.; Zhang, H.; Qin, J.; Shi, X.; Fang, X. Microcellular epoxy/reduced graphene oxide/multi-walled carbon nanotube nanocomposite foams for electromagnetic interference shielding. *Appl. Surf. Sci.* **2021**, *552*, 149232.
(25) Yang, C.; Chen, N.; Liu, X.; Wang, Q.; Zhang, C. Coupling selective laser sintering and supercritical CO_2 foaming for 3D printed porous polyvinylidene fluoride with improved piezoelectric performance. *RSC Adv.* **2021**, *11*, 20662−20669.
(26) Zou, C.; Yang, K.; Wang, K.; Pei, X.; Dong, Z.; Hong, Y.; Zhang, X. Combination of fused deposition modeling and gas foaming technique to fabricated hierarchical macro/microporous polymer scaffolds. *Mater. Des.* **2016**, *109*, 415−424.
(27) Lu, L.; Ding, W.; Liu, J.; Yang, B. Flexible PVDF based piezoelectric nanogenerators. *Nano Energy* **2020**, *78*, 105251.
(28) Widakdo, J.; Chiao, Y. H.; Lai, Y. L.; Imawan, A. C.; Wang, F. M.; Hung, W. S. Mechanism of a Self-Assembling Smart and Electrically Responsive PVDF-Graphene Membrane for Controlled Gas Separation. *ACS Appl. Mater.* **2020**, *12*, 30915−30924.
(29) Shi, K.; Chai, B.; Zou, H.; Shen, P.; Sun, B.; Jiang, P.; Shi, Z.; Huang, X. Interface induced performance enhancement in flexible $BaTiO_3$/PVDF-TrFE based piezoelectric nanogenerators. *Nano Energy* **2021**, *80*, 105515.
(30) Yang, L.; Wang, L.; Chen, Y. Solid-state shear milling method to prepare PA12/boron nitride thermal conductive composite powderss and their selective laser sintering 3D-printing. *Appl. Polym. Sci.* **2020**, *137*, 48766.
(31) Song, S.; Li, Y.; Bai, S.; Wang, Q. Production of spherical polymeric composite powders for selective laser sintering via plasma assisted solid state shear milling: From theory to piezoelectric application. *Chem. Eng. J.* **2021**, *415*, 129035.
(32) Chung, H.; Das, S. Processing and properties of glass bead particulate-filled functionally graded Nylon-11 composites produced by selective laser sintering. *A-Structural Mat.* **2006**, *437*, 226−234.
(33) Yan, M.; Tian, X.; Peng, G.; Li, D.; Zhang, X. High temperature rheological behavior and sintering kinetics of CF/PEEK composites during selective laser sintering. *Compos. Sci. Technol.* **2018**, *165*, 140−147.
(34) Fanselow, S.; Emamjomeh, S. E.; Wirth, K.-E.; Schmidt, J.; Peukert, W. Production of spherical wax and polyolefin microparticles by melt emulsification for additive manufacturing. *Chem. Eng. Sci.* **2016**, *141*, 282−292.
(35) Lee, J. E.; Leung, S. N. Multi-stage crystallization mechanism of electroactive phase polyvinylidene fluoride induced by thermal and supercritical carbon dioxide processing. *CrystEngComm* **2018**, *20*, 4080−4089.
(36) Zhu, G. D.; Zeng, Z. G.; Zhang, L.; Yan, X. J. Piezoelectricity in β-phase PVDF crystals: A molecular simulation study. *Comput. Mater. Sci.* **2008**, *44*, 224−229.
(37) Martins, P.; Lopes, A. C.; Lanceros-Mendez, S. Electroactive phases of poly(vinylidene fluoride): Determination, processing and applications. *Prog. Polym. Sci.* **2014**, *39*, 683−706.
(38) Fan, B.; Bai, J. Composites of hybrids $BaTiO_3$/carbon nanotubes/polyvinylidene fluoride with high dielectric properties. *J. Phys. D.* **2015**, *48*, 455303.
(39) Xiang, Y. H.; Xue, L. X.; Shen, J. H.; Lin, H. B.; Liu, F. Effect of Solvents on Morphology and Polymorphism of Polyvinylidene Fluoride Membrane via Supercritical CO_2 Induced Phase Separation. *J. Appl. Polym. Sci.* **2014**, *131*, 41065.
(40) Shen, L.; Gong, L.; Chen, S.; Zhan, S.; Zhang, C.; Shao, T. Improvement of β-phase crystal formation in a $BaTiO_3$-modified PVDF membrane. *Plasma Science and Technology* **2018**, *20*, No. 065510.
(41) Lee, C.; Tarbutton, J. A. Electric poling-assisted additive manufacturing process for PVDF polymer-based piezoelectric device applications. *Smart Mater. Struct.* **2014**, *23*, No. 095044.
(42) Fan, Y.; Huang, X.; Wang, G.; Jiang, P. Core−Shell Structured Biopolymer@$BaTiO_3$ Nanoparticles for Biopolymer Nanocomposites with Significantly Enhanced Dielectric Properties and Energy Storage Capability. *J. Phys. Chem. C* **2015**, *119*, 27330−27339.
(43) Xu, C. W.; Zhang, L.; Xu, Y. L.; Yin, Z. Z.; Chen, Q.; Ma, S. Y.; Zhang, H. H.; Huang, R.; Zhang, C. L.; Jin, L.; Yang, W. Q.; Lu, J. Filling the holes in piezopolymers with a solid electrolyte: a new paradigm of poling-free dynamic electrets for energy harvesting. *J. Phys. Chem. A.* **2017**, *5*, 189−200.
(44) Moody, M. J.; Marvin, C. W.; Hutchison, G. R. Molecularly-doped polyurethane foams with massive piezoelectric response. *J. Phys. Chem. C* **2016**, *4*, 4387−4392.
(45) Yang, C.; Song, S.; Chen, F.; Chen, N. Fabrication of PVDF/$BaTiO_3$/CNT Piezoelectric Energy Harvesters with Bionic Balsa Wood Structures through 3D Printing and Supercritical Carbon Dioxide Foaming. *ACS Appl. Mater.* **2021**, *13*, 41723−41734.
(46) Kim, H. J.; Kim, Y. J. High performance flexible piezoelectric pressure sensor based on CNT-sdoped 0-3 ceramic-epoxy nanocomposites. *Mater. Des.* **2018**, *151*, 133−140.
(47) Jiang, J.; Tu, S.; Fu, R.; Li, J.; Hu, F.; Yan, B.; Gu, Y.; Chen, S. Flexible Piezoelectric Pressure Tactile Sensor Based on Electrospun $BaTiO_3$/Poly(vinylidene fluoride) Nanocomposite Membrane. *ACS Appl. Mater.* **2020**, *12*, 33989−33998.
(48) Yang, Y.; Pan, H.; Xie, G.; Jiang, Y.; Chen, C.; Su, Y.; Wang, Y.; Tai, H. Flexible piezoelectric pressure sensor based on polydopamine-modified $BaTiO_3$/PVDF composite film for human motion monitoring. *Sens. Actuator A Phys.* **2020**, *301*, 111789.
(49) Kim, H.; Lee, D.; Kim, D.; Kong, D.; Choi, J.; Lee, M.; Murillo, G.; Jung, J. Dominant Role of Young's Modulus for Electric Power Generation in PVDF-$BaTiO_3$ Composite-Based Piezoelectric Nanogenerator. *Nanomaterials-Basel* **2018**, *8*, 777.
(50) González-Benito, J.; Olmos, D.; Martinez-Tarifa, J. M.; González-Gaitano, G.; Sánchez, F. A. PVDF/$BaTiO_3$/carbon nanotubes ternary nanocomposites prepared by ball milling: Piezo and dielectric responses. *J. Appl. Polym. Sci.* **2019**, *136*, 47788.
(51) Yaqoob, U.; Uddin, A. S. M. I.; Chung, G. S. A novel tri-layer flexible piezoelectric nanogenerator based on surface-modified graphene and PVDF-$BaTiO_3$ nanocomposites. *Appl. Surf. Sci.* **2017**, *405*, 420−426.
(52) Tabhane, G. H.; Giripunje, S. M. Robust flower-like ZnO assembled β-PVDF/BT hybrid nanocomposite: Excellent energy harvester. *Polym. Test.* **2020**, *88*, 106564.
(53) Xu, D.; Zhang, H.; Pu, L.; Li, L. Fabrication of Poly(vinylidene fluoride)/Multiwalled carbon nanotube nanocomposite foam via supercritical fluid carbon dioxide: Synergistic enhancement of piezoelectric and mechanical properties. *Compos. Sci. Technol.* **2020**, *192*, 108108.
(54) Kim, S. H.; Ha, J. W.; Lee, S. G.; Sohn, E. H.; Park, I. J.; Kang, H. S.; Yi, G. R. Fluorinated Titania Nanoparticle-Induced Piezo-

https://doi.org/10.1021/acsomega.1c04998
ACS Omega 2021, 6, 30769−30778

electric Phase Transition of Poly(vinylidene fluoride). *Langmuir* **2019**, *35*, 8816−8822.
(55) Soin, N.; Boyer, D.; Prashanthi, K.; Sharma, S.; Narasimulu, A. A.; Luo, J.; Shah, T. H.; Siores, E.; Thundat, T. Exclusive self-aligned *β*-phase PVDF films with abnormal piezoelectric coefficient prepared via phase inversion. *Chem. Commun.* **2015**, *51*, 8257−8260.

https://doi.org/10.1021/acsomega.1c04998
ACS Omega 2021, 6, 30769−30778